Electronic Supplementary Information

Covalent Organic Frameworks Based on Tetraphenyl-*p*-Phenylenediamine and Metalloporphyrin for Electrochemical Conversion of CO₂ to CO

Lei Gong, Baotong Chen, Ying Gao, Baoqiu Yu, Yinhai Wang, Bin Han, Chenxiang Lin, Yongzhong Bian, Dongdong Qi and Jianzhuang Jiang

Beijing Key Laboratory for Science and Application of Functional Molecular and Crystalline Materials, Department of Chemistry, School of Chemistry and Biological Engineering, University of Science and Technology Beijing, Beijing 100083, China

Daxing Research Institute, and Beijing Advanced Innovation Center for Materials Genome Engineering, University of Science and Technology Beijing, Beijing 100083, China

Guangxi Key Laboratory of Natural Polymer Chemistry and Physics, Nanning Normal University, Nanning 530001, China

Contents

electrocatalysis.

TPPDA-CoPor-COF and CoPor monomer.

EXPERIMENTAL SECTION

Materials

CoPor and NiPor were synthesized following the published procedure[1]. All other regents were commercially available and used as received.

Characterization

NMR spectra were recorded on a Bruker DPX 400 spectrometer (^{1}H: 400 MHz) in D_2O with dimethyl sulfoxide (DMSO) used as an internal standard. Powder X-ray diffraction (PXRD) was collected at room temperature on a PANalytical Empyrean series 3 diffractometer equipped with Cu K_α radiation. FT-IR spectra were recorded as KBr pellets using a Bruker Tensor 37 spectrometer with 4 cm^{-1} resolution. X-ray photoelectron spectroscopy (XPS) data were recorded on a Thermo Scientific K-Alpha system. Al K_α X-ray (6 mA / 12 KV) was utilized as the irradiation source. All XPS measurements were performed in the CAE mode with the reference of C 1s (284.8 eV). The nitrogen adsorption and desorption isotherms were measured at 77 K and the CO_2 adsorption and desorption isotherms were measured at 298 K using a Micromeritics ASAP 2020 PLUS HD88 system. The samples were degassed at 90°C for 4 hours before the measurements. The thermogravimetric analysis (TGA) was performed on a Rigaku TG-DTA8122 instrument under nitrogen atmosphere with a heating rate of 10°C/min. XAFS measurements were obtained at 4B9A beamline of Beijing Synchrotron Radiation Facility (BSRF). The storage ring of BSRF was operated at 2.5

GeV with a maximum current of 250 mA and all spectra were collected in ambient conditions, using fluorescence mode. XAFS data processing and fitting were conducted on IFEFFIT program package. The metal contents of TPPDA-CoPor-COF and TPPDA-NiPor-COF were determined by inductively coupled plasma (ICP) analysis with an Aglient 5110 ICP-OES instrument. Energy dispersive spectroscopy (EDS) mapping images were collected by transmission electron microscopy (JEM-2100F) at an operation voltage of 200 kV. Scanning electron microscopy (SEM) images were obtained on a HITACHI SU8010 microscope. AFM images were measured by a Bruker Multimode 8 system with a silicon cantilever by using tapping mode. UV-vis diffuse reflectance absorption spectra (DRS) were recorded on a Shimadzu UV-2600 spectrophotometer with $BaSO_4$ as the reference.

Synthesis of TPPDA-CoPor-COF

CoPor (18.8 mg, 0.024 mmol), TPPDA (11.4 mg, 0.024 mmol), n-butanol (0.36 mL), o-dichlorobenzene (1.44 mL), and 6 M aqueous acetic acid (0.18 mL) were mixed in a Pyrex tube (9 × 6 mm, o.d. × i.d.). After sonication for 10 min, the Pyrex tube was subjected to freeze degassing for three times. Then the tube was sealed and placed in an oven at 120°C for 72 h. The obtained COFs was placed in a Soxhlet Extractor and washed with tetrahydrofuran (24 h) and chloroform (24 h) in turn. Finally, the product was dried under vacuum at 70°C for 12 h to provide TPPDA-CoPor-COF (23.6 mg, 78%).

Synthesis of TPPDA-NiPor-COF

TPPDA-NiPor-COF (24.2 mg, 80%) was synthesized following the similar procedure for TPPDA-CoPor-COF, except that CoPor was replaced with NiPor.

Preparation of TPPDA-CoPor-COF nanosheets

The as-prepared TPPDA-CoPor-COF (20.0 mg) was added into a beaker with deionized water (80 mL) and then high-frequency (600 W) sonication was performed for 60 min at 25°C. After filtration (filter paper, ~220 nm), the obtained sample was collected and dried under vacuum at 60°C for 12 h.

Electrochemical measurements.

All electrocatalysis tests were conducted at room temperature in a standard three-electrode configuration using H-type cell on the electrochemical workstation (chi760E). In the H-type cell, two compartments equipped with 0.5 M $KHCO_3$ aqueous solution were separated by an anion exchange membrane (Nafion-117). Ag/AgCl electrode and Pt foil were served as the reference and counter electrodes, respectively. A catalyst-modified carbon fiber paper electrode was used as the work electrode.

TPPDA-MPor-COFs or CoPor/TPPDA (5 mg), Vulcan XC-72R carbon black (5 mg), ethanol (965 μL) and Nafion perfluorinated resin solution (35 μL, 10 wt. % in H_2O) were mixed in a vial. Homogeneous pastes were formed after sonication for 60 min. To make sure that loading density of the catalyst was 1 mg cm^{-2}, 100 μL paste was dropped evenly onto a piece of carbon fiber paper (1 cm × 1 cm). The catalyst-modified carbon fiber paper electrode was placed in dark for 12 h. Before each

electrochemical test, the electrolyte solution was saturated with Ar or CO_2 for 30 min. Linear sweep voltammetry (LSV) polarization curves were measured from 0 to −1.63 V vs Ag/AgCl with a scan rate of 10 mV s^{-1}. On account of the following equation: E (vs RHE) = E (vs Ag/AgCl) + 0.197 V + 0.059 × pH, the results of electrocatalysis in this work were presented vs RHE. Besides, no *iR* compensation was carried out for all LSV polarization curves.

EIS spectroscopies were measured under an AC voltage of −1.5 V vs Ag/AgCl with 5 mV amplitude in a frequency range from 1000 kHz to 100 mHz. Cyclic voltammograms (CV) tests were conducted to obtain C_{dl} under the potential window from 0.14 to 0.04 V vs RHE with various scan rates from 10 to 100 mV s^{-1} to estimate the ECSA.

Structure modeling

The unit cells of the models were refined with the experimental PXRD data of TPPDA-CoPor-COF by using the Le Bail refinement. The cell parameters and the refined PXRD patterns were obtained until the values of R_{wp} and R_p converged.

DFT calculation methods

Density functional theory (DFT) calculations were performed by PBE0-D3 method with Becke-Johnson damping.[2,3] A mixed basis set, including 6-31G(d) for C/H/N/O and SDD for Co/Ni, was utilized to optimize the structures and calculate the Gibbs free energies using Gaussian 09 program (version D.01).[4-8] Mulliken charge of central metal

atom was carried out based on the DFT calculated results. Besides, the solvation model based on density (SMD) was used to simulate the aqueous environment.[9]

The electrocatalytic mechanisms were studied based on Nøskov's computational hydrogen electrode model.[10,11] In this technique, zero voltage was defined based on the potential energy (μ) of components involved in the reversible hydrogen electrode at all pH, T and p, therefore, $\mu(H^+) + \mu(e-) = \frac{1}{2}\mu(H_2)$ at a potential of 0 V. The pathways adopted for CO_2 reduction to CO in this work are listed below (the asterisks represent the active sites):

* + CO_2 + H^+ +e^-→ *COOH

*COOH + H^++ e^-→*CO + H_2O

CO → + CO
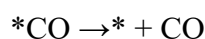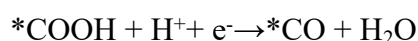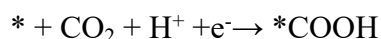
In addition, the pathway adopted for hydrogen evolution reaction (HER) in this work is shown as below (the asterisks represent the active sites):

* + H^+ + e^-→ *H
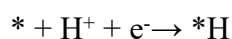
Calculation of Faradaic Efficiency

The Faradaic efficiencies (FE) for CO production at each applied potential were calculated based on the following equation:

$$FE = \frac{j_{CO}}{j_{total}} = \frac{v_{CO} \times N \times F}{j_{total}}$$

FE: Faradaic efficiency for CO production (%); j_{CO}: partial current density for CO production; j_{total}: total current density; v_{CO}: the production rate of CO; N: the number of electrons (Here, it is 2 for CO); F: Faradaic constant, 96485 C mol^{-1}.

Calculation of Turnover Frequency (TOF, s^{-1})

The TOF for CO was calculated based on the following equation:

$$TOF = \frac{j_{total} \times FE_{CO} / NF}{\omega m_{cat} / M}$$

j_{total}: total current density; FE_{CO}: Faradaic efficiency for CO production (%); N: the number of electrons (Here, it is 2 for CO); F: Faradaic constant, 96485 C mol^{-1}; ω: the metal content of Co or Ni; m_{cat}: the catalyst mass in the electrode; M: the atomic mass of Co or Ni.
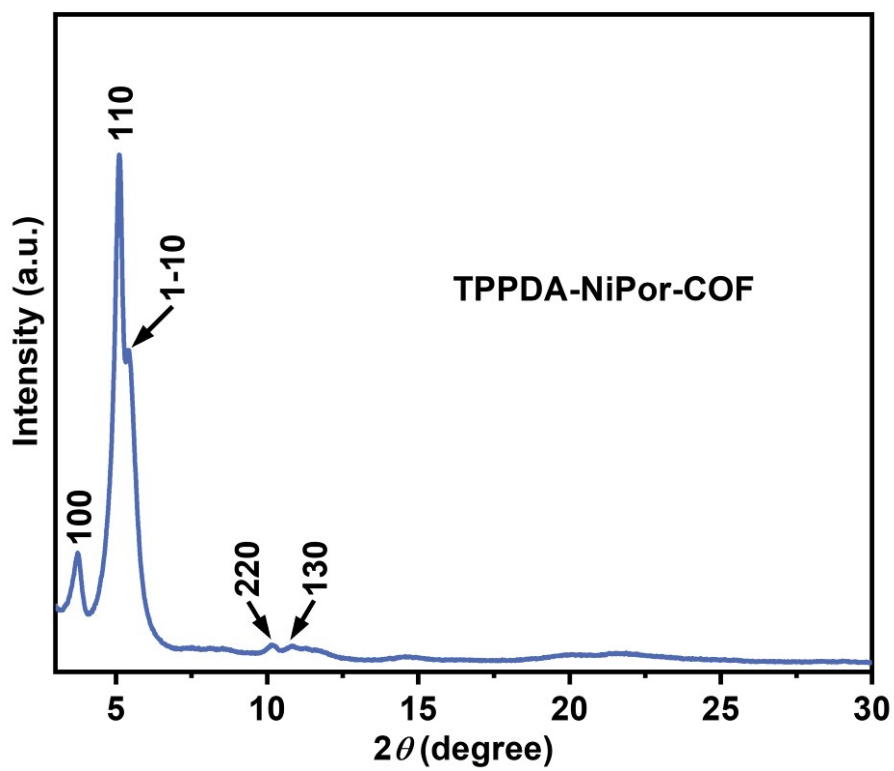
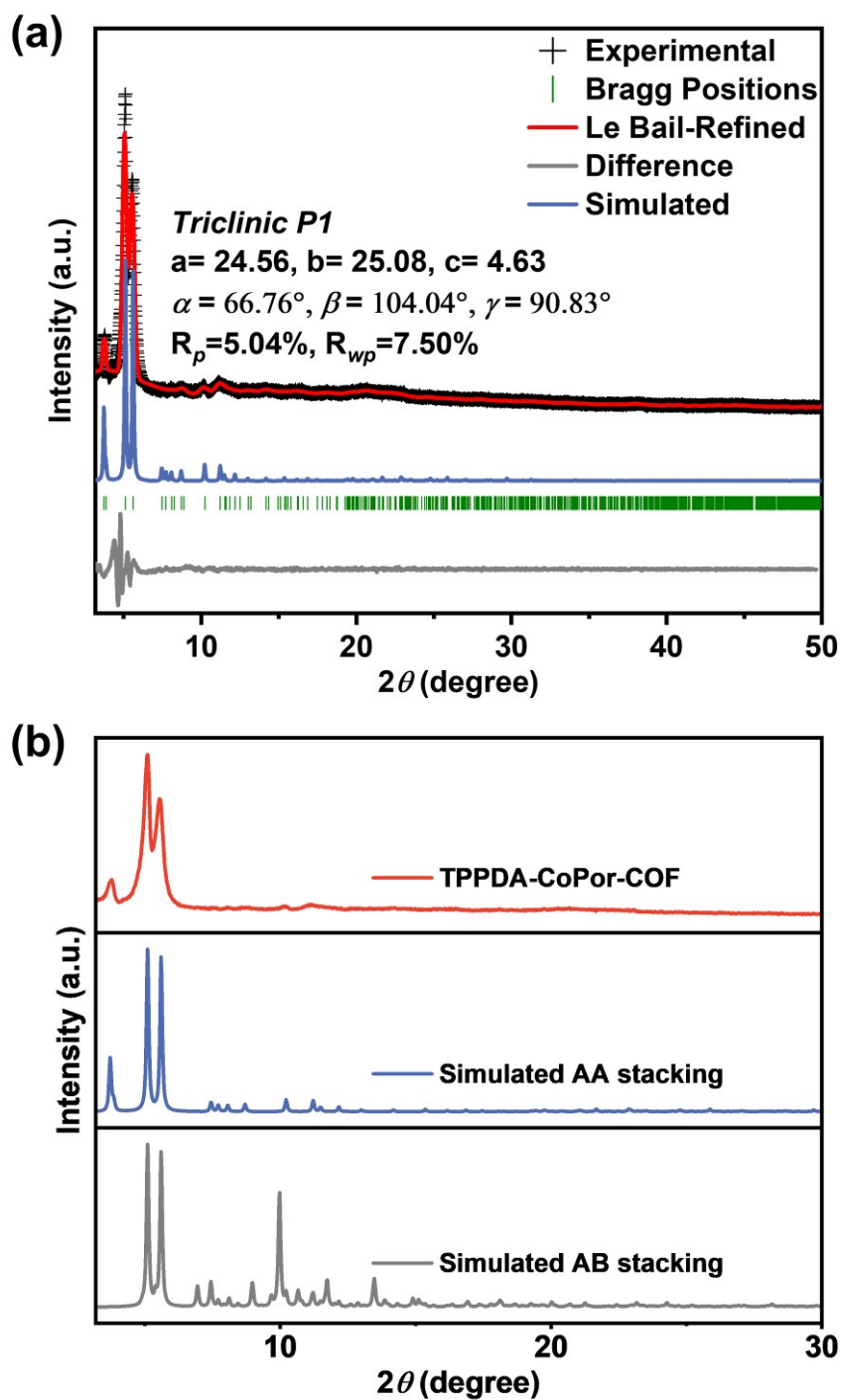**Fig. S1.** The experimental PXRD pattern of TPPDA-NiPor-COF.

Fig. S2. (a) Experimental, Le Bail refined and simulated PXRD patterns, (b) Experimental and simulated (AA and AB stacking) PXRD patterns of TPPDA-CoPor-COF.
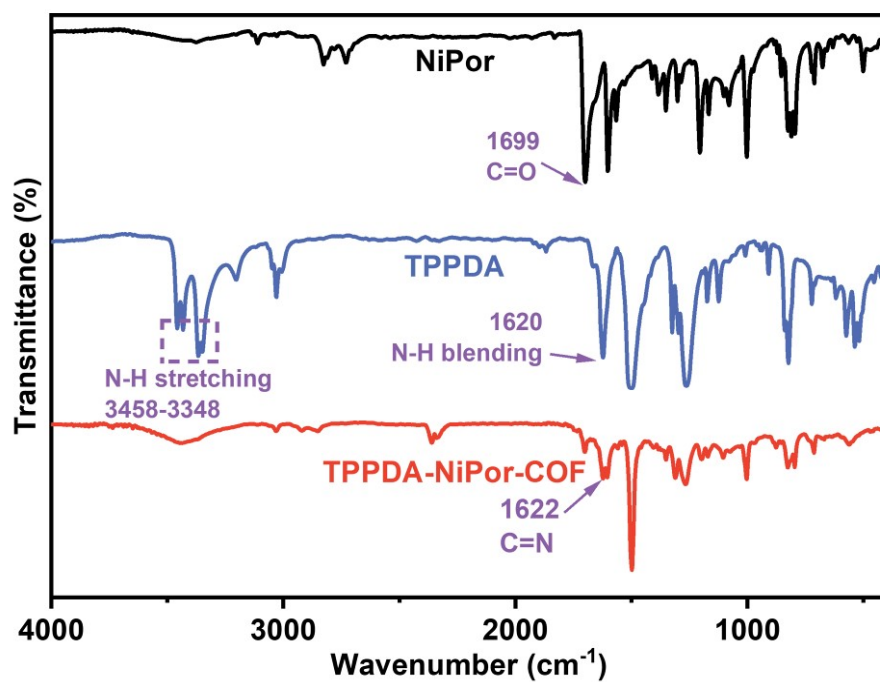
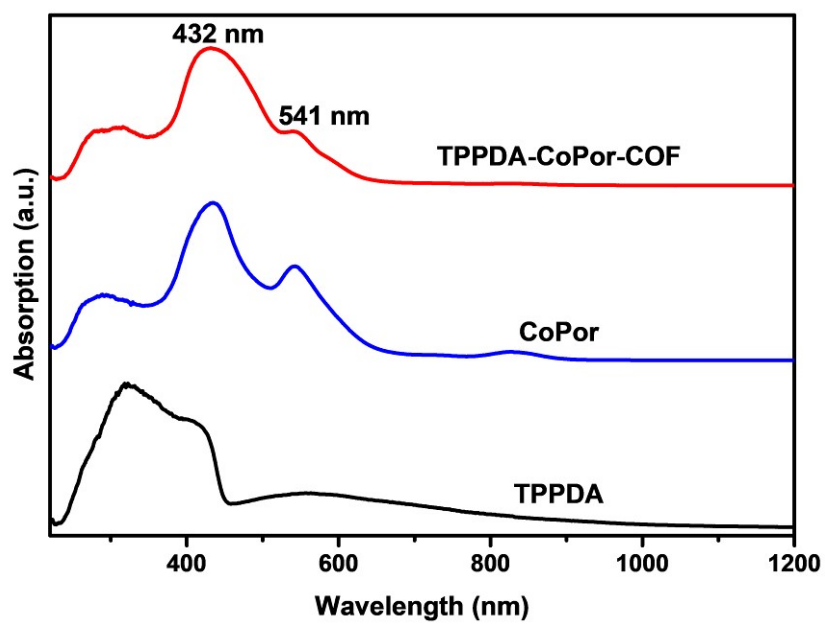**Fig. S3.** FT-IR spectra of TPPDA-NiPor-COF, TPPDA and NiPor.

Fig. S4. The solid state diffuse reflectance electronic absorption spectrum of TPPDA-CoPor-COF, CoPor and TPPDA.
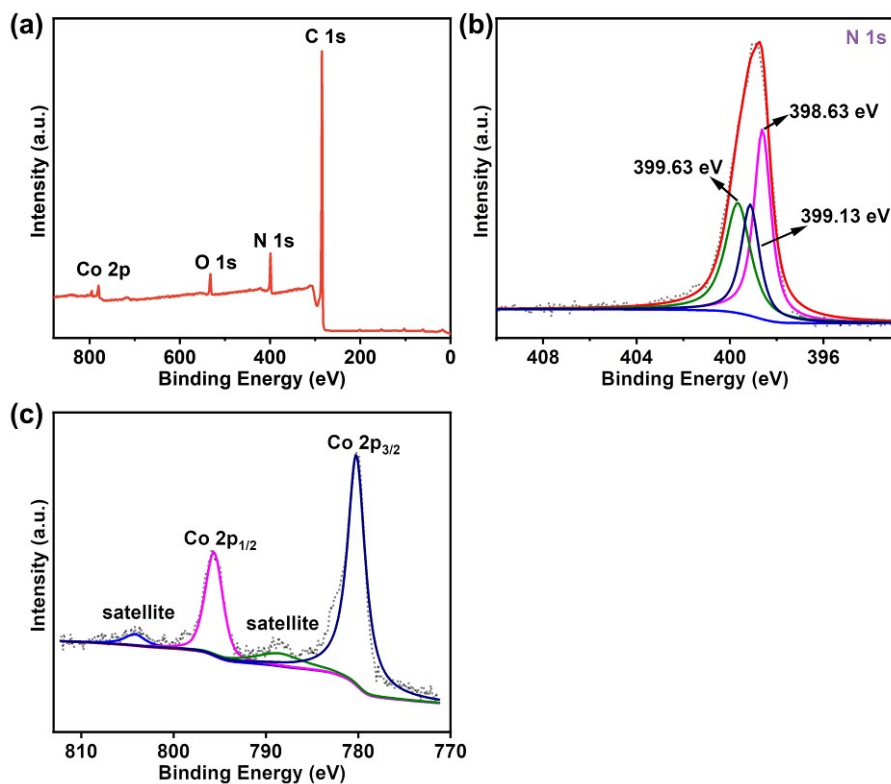
Fig. S5. High-resolution XPS spectra of TPPDA-CoPor-COF. (a) Total XPS spectrum of TPPDA-CoPor-COF. (b) High-resolution scan of N 1s. (c) High-resolution scan of Co 2p.
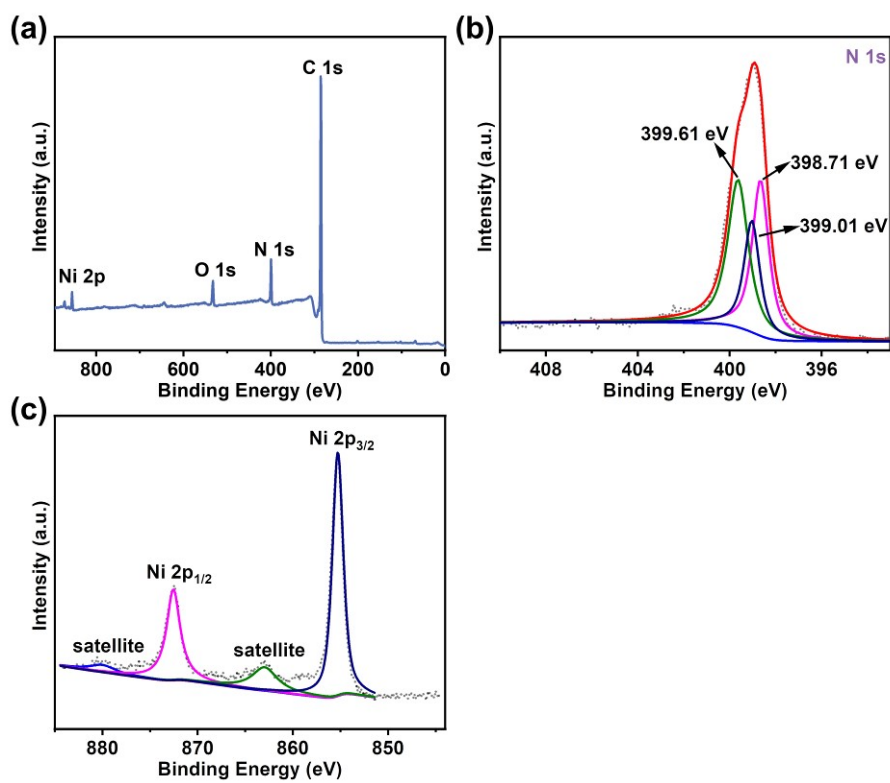
Fig. S6. High-resolution XPS spectra of TPPDA-NiPor-COF. (a) Total spectrum of TPPDA-NiPor-COF. (b) High-resolution scan of N 1s. (c) High-resolution scan of Ni 2p.
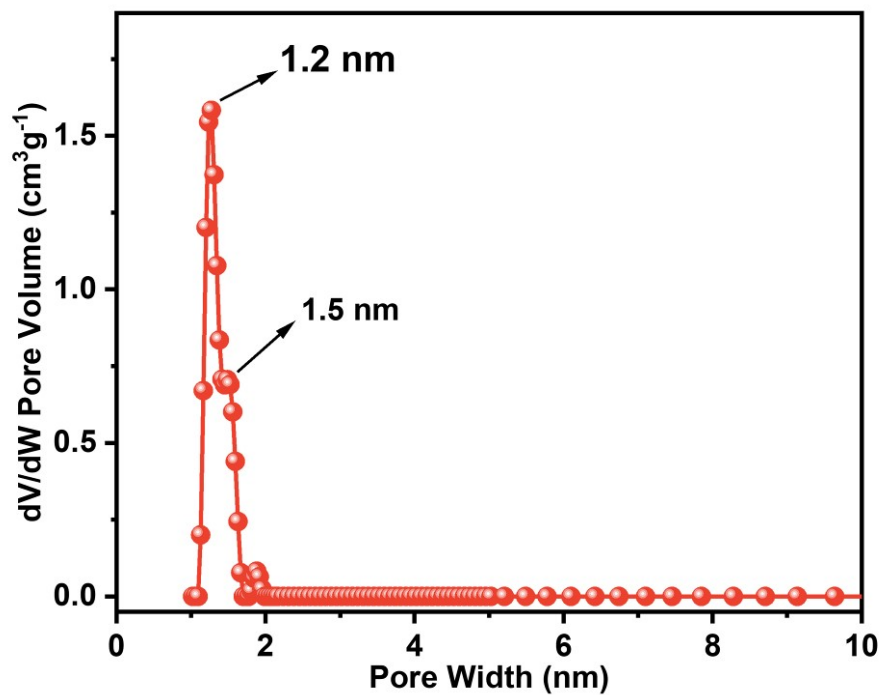
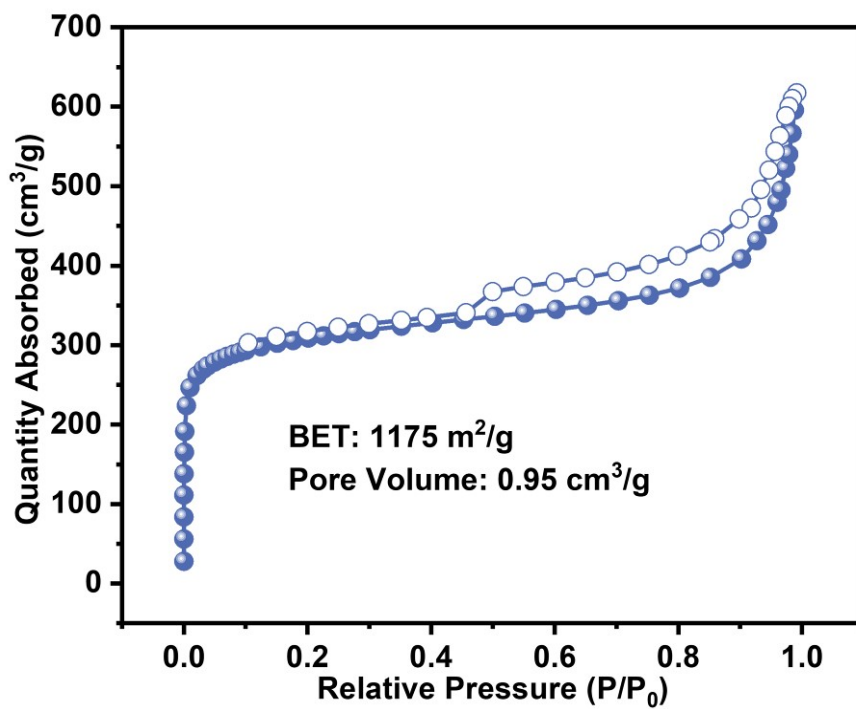**Fig. S7.** Pore size distribution of TPPDA-CoPor-COF.
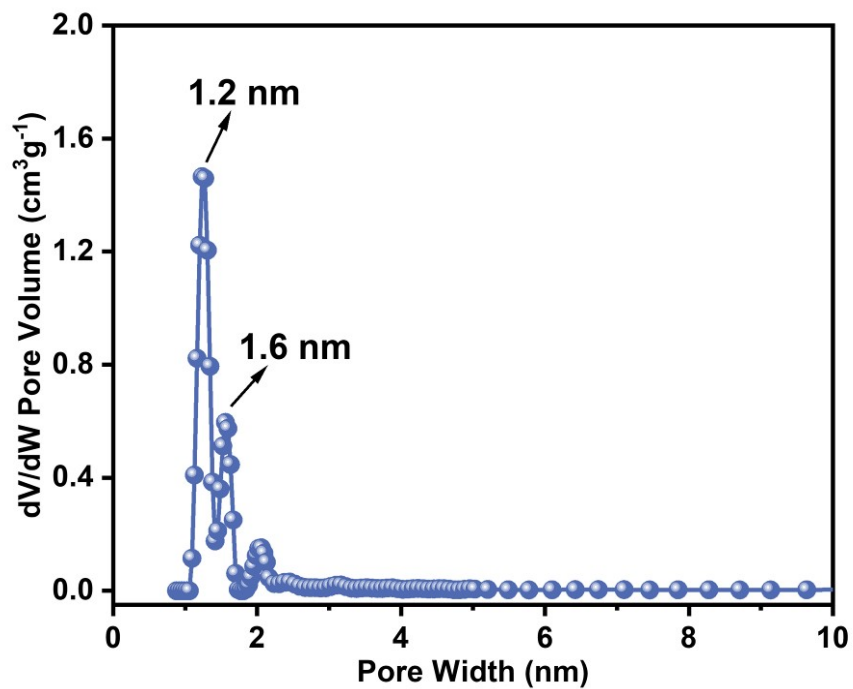

Fig. S8. N$_2$ sorption isotherm of TPPDA-NiPor-COF at 77 K.

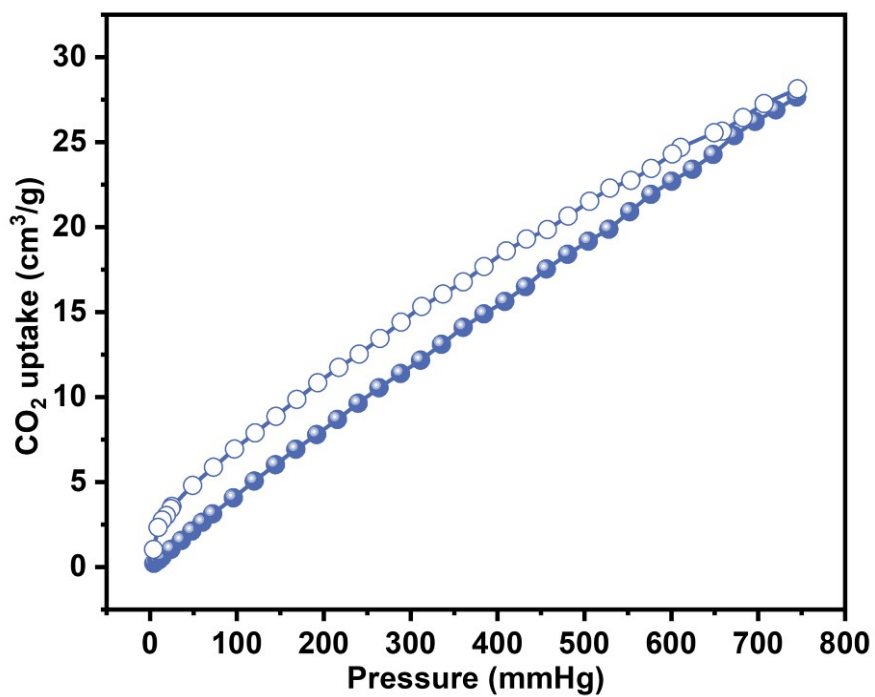**Fig. S9.** Pore size distribution of TPPDA-NiPor-COF.

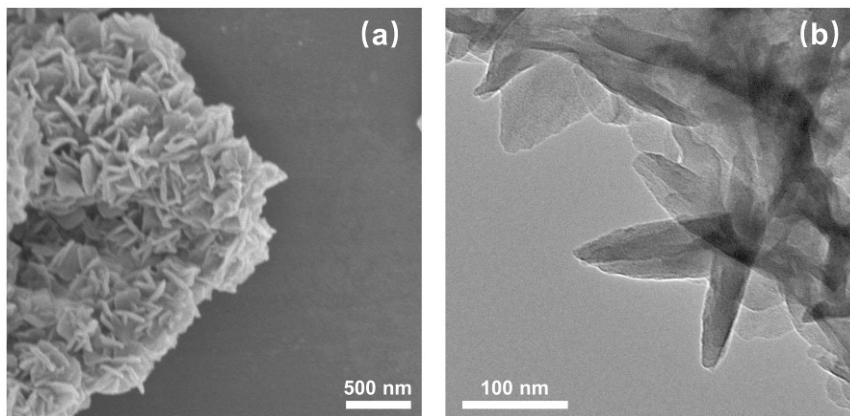**Fig. S10.** CO_2 sorption isotherm of TPPDA-NiPor-COF at 298 K.

Fig. S11. (a) SEM and (b) TEM images of TPPDA-NiPor-COF.
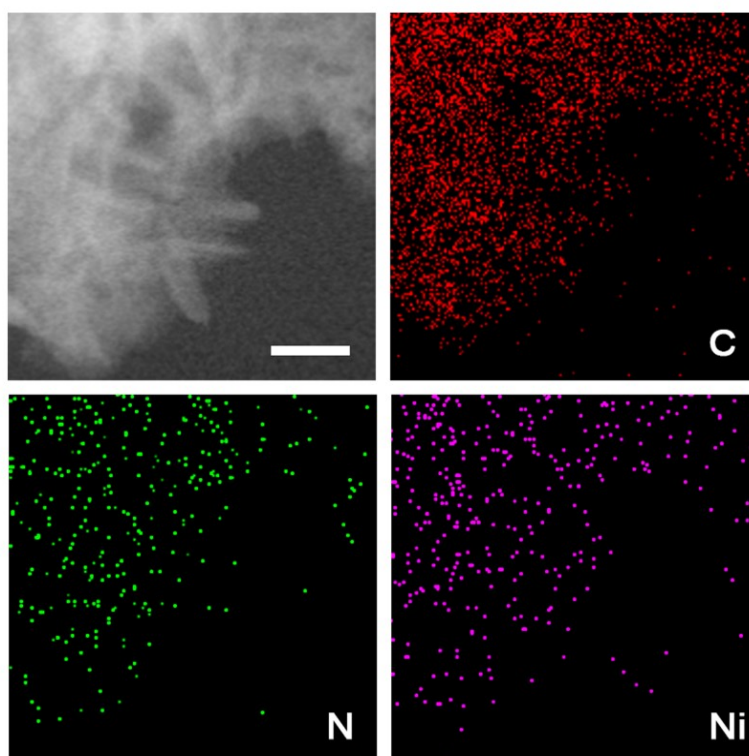

Fig. S12. EDS mappings of TPPDA-NiPor-COF (scale bar = 250 nm).

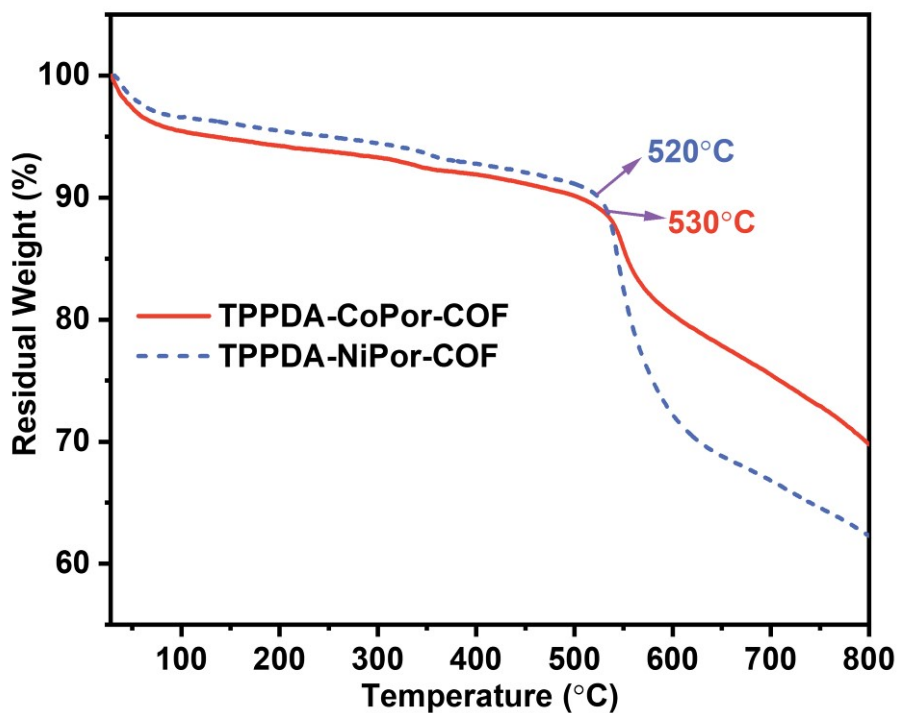**Fig. S13.** TG curves of TPPDA-CoPor-COF and TPPDA-NiPor-COF, with a constant heating rate of 10°C min^{-1} from 30 to 800°C in N_2.
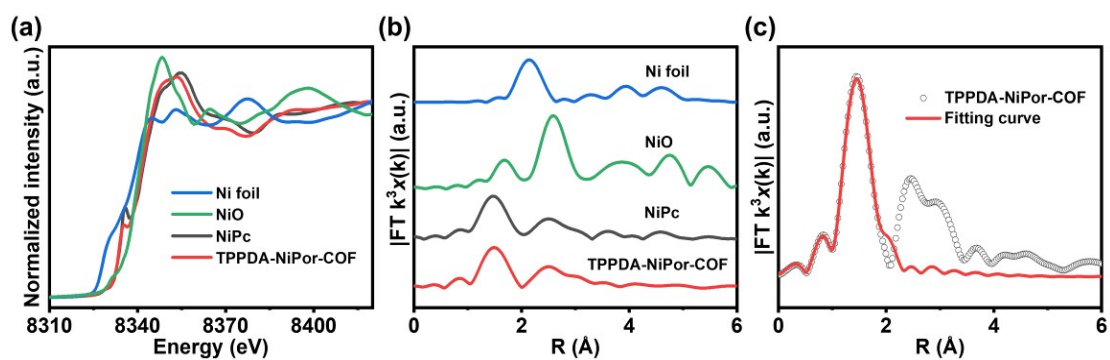
Fig. S14. (a) Normalized Ni K-edge XANES spectra of Ni foil, NiO, NiPc and TPPDA-NiPor-COF. (b) Fourier transform EXAFS spectra of Ni foil, NiO, NiPc, and TPPDA-NiPor-COF. (c) The corresponding EXAFS fitting curve of TPPDA-NiPor-COF.
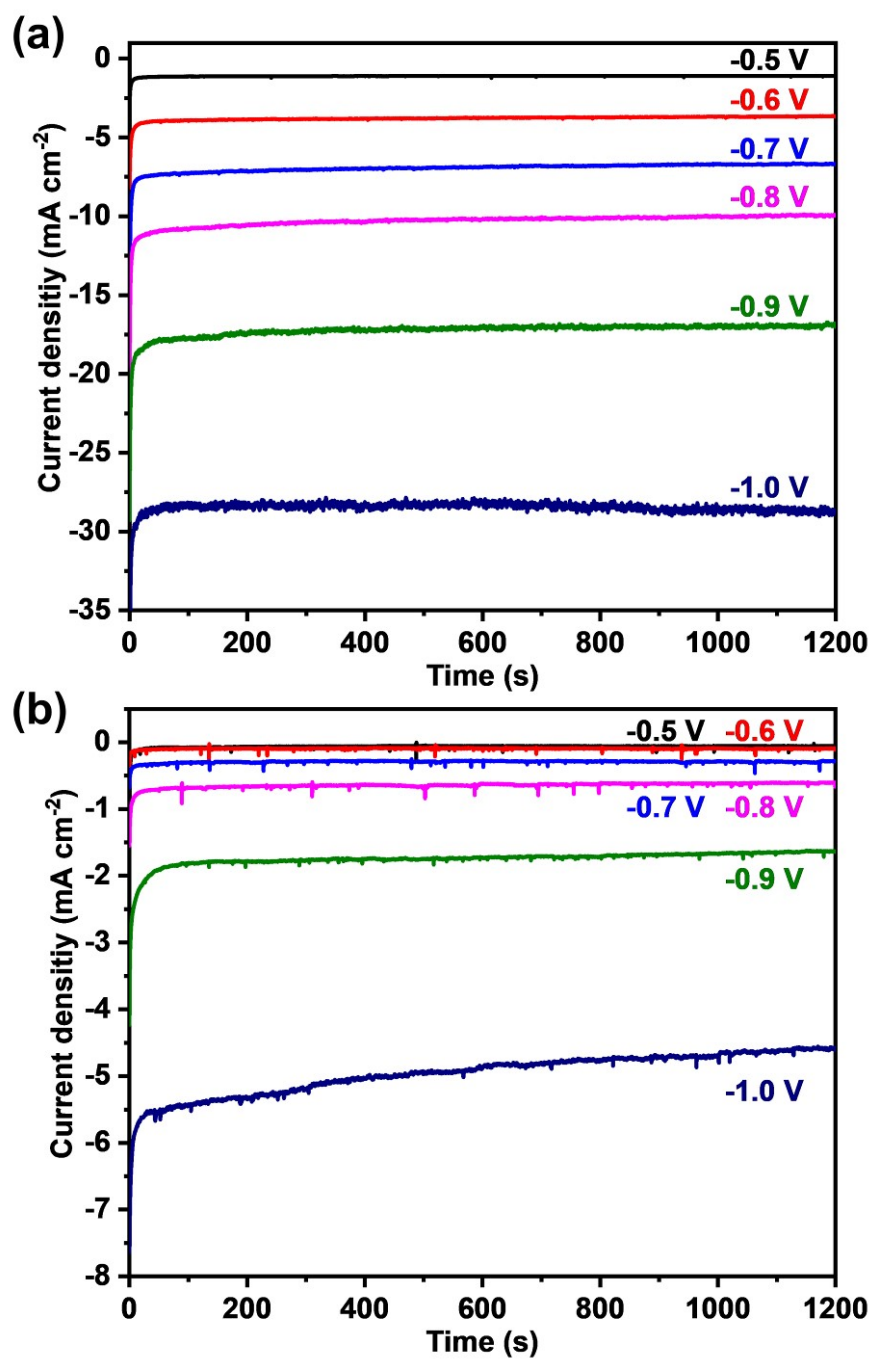
Fig. S15. Chronoamperometric responses of TPPDA-CoPor-COF (a) and TPPDA-NiPor-COF (b) at different potentials vs RHE.
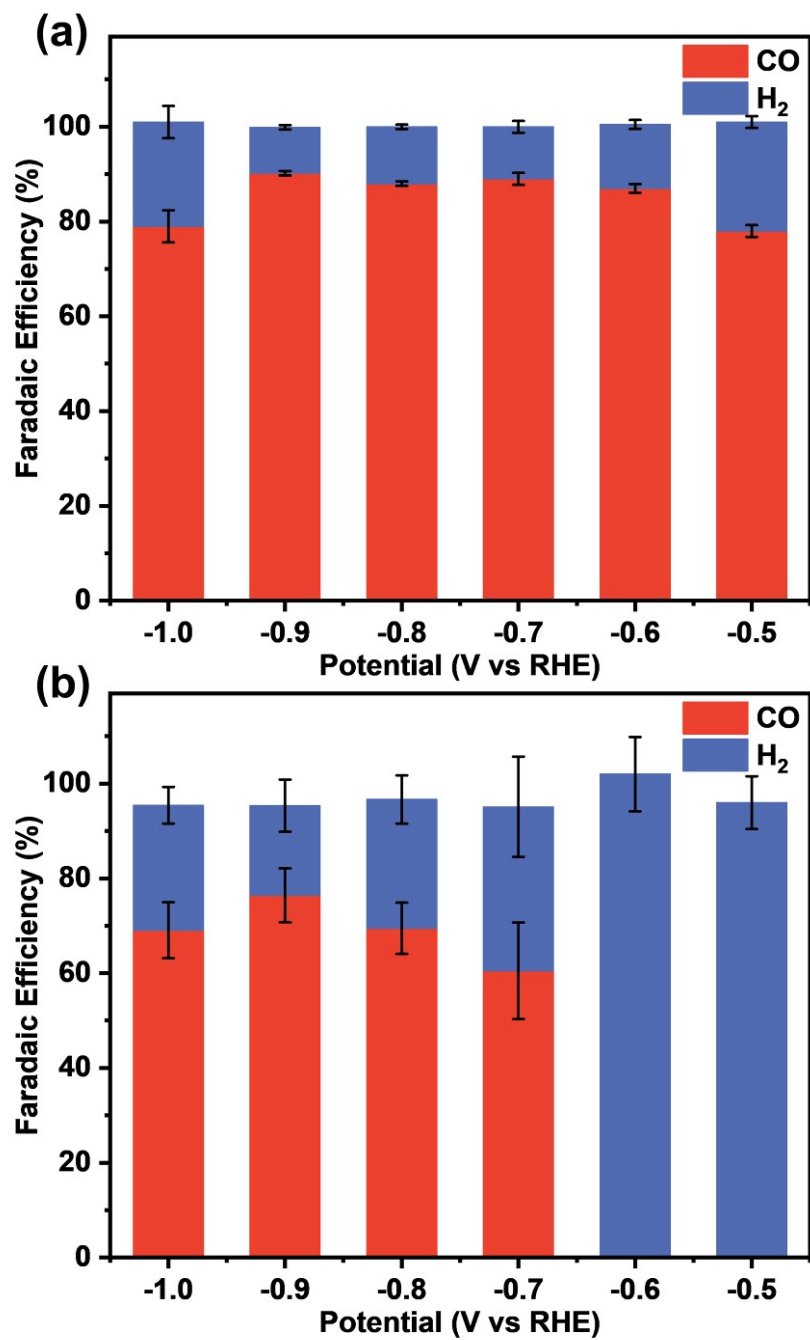
Fig. S16. Faradic efficiency of TPPDA-CoPor-COF (a) and TPPDA-NiPor-COF (b) at different potentials vs RHE.
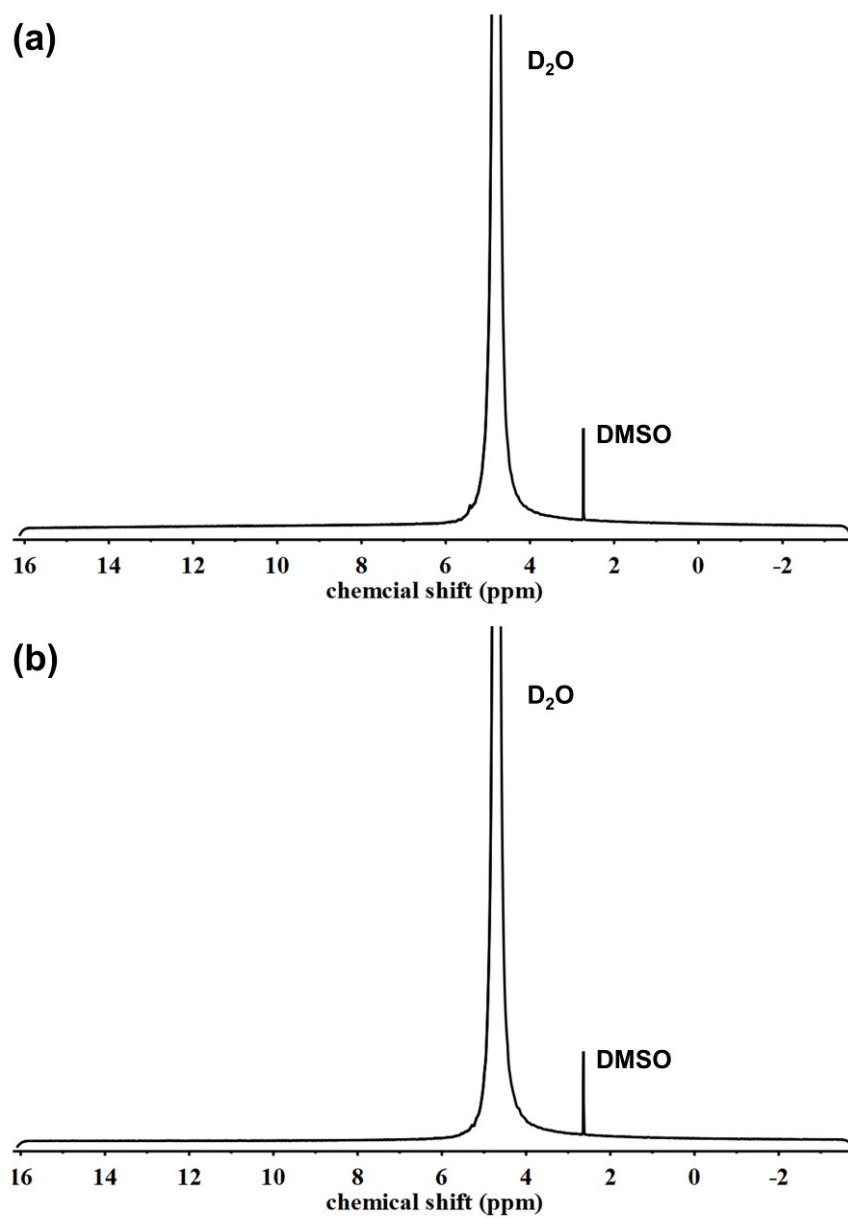
Fig. S17. ^{1}H NMR spectra of the electrolytes after continuous CO_2RR tests in D_2O.

TPPDA-CoPor-COF (a) and TPPDA-NiPor-COF (b).
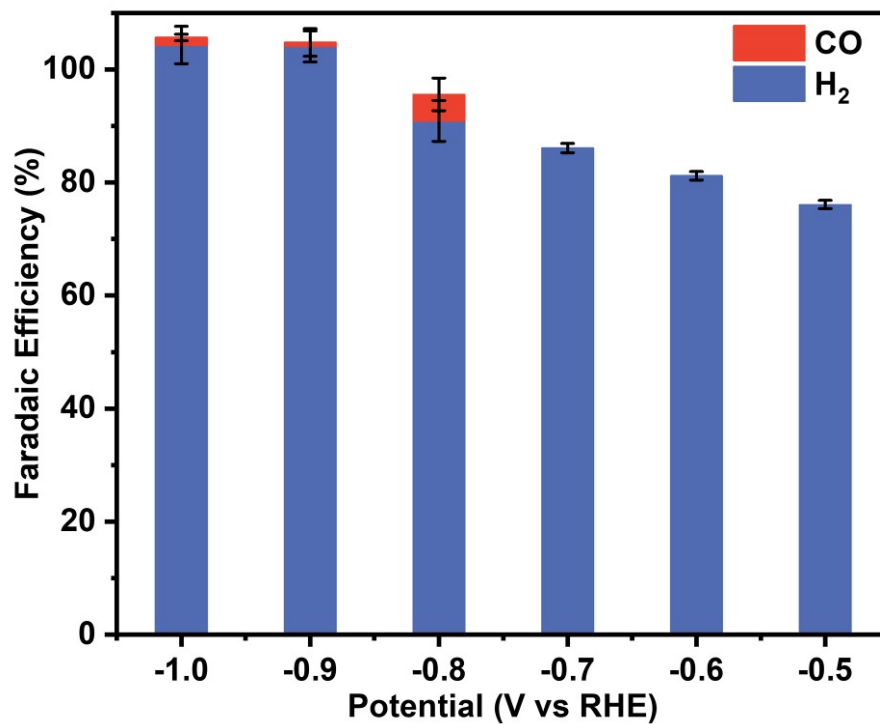
Fig. S18. FE_{CO} and FE_{H_2} of TPPDA-CoPor-COF at different applied potentials in Ar-saturated 0.5 M $KHCO_3$.
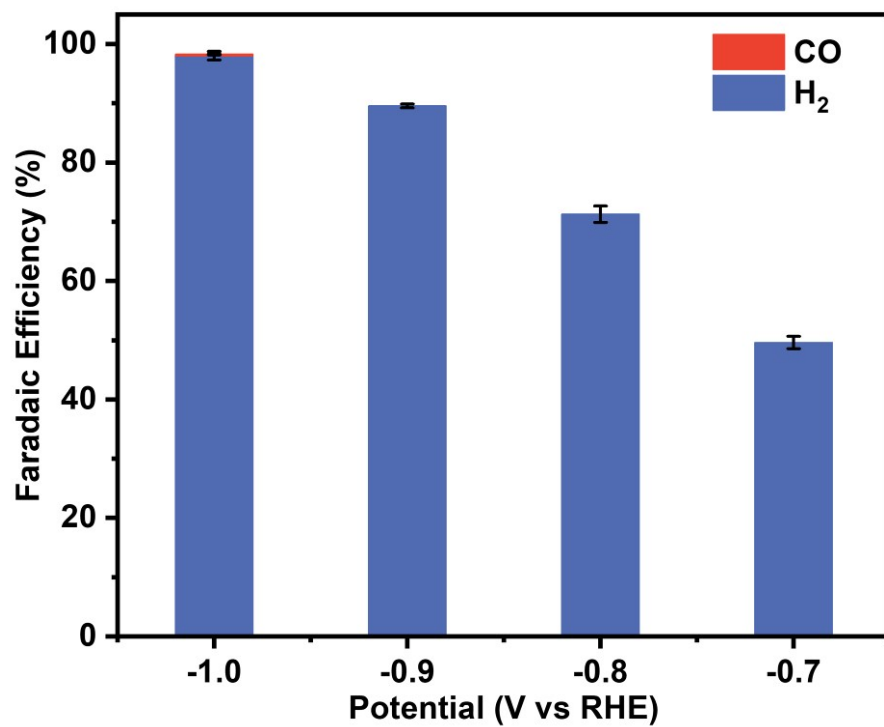
Fig. S19. FE_{CO} and FE_{H_2} of the carbon cloth with Vulcan XC-72R carbon black and Nafion at different applied potentials in CO_2 saturated 0.5 M $KHCO_3$.
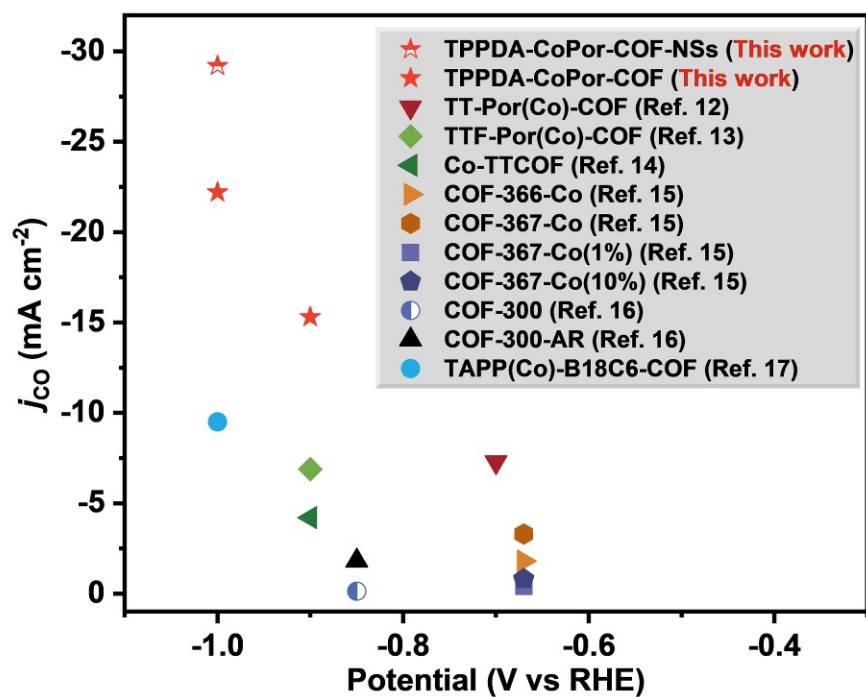
Fig. S20. Comparison of j_{CO} values for COF-based electrocatalysts in H-cells (0.5 M KHCO$_3$ aqueous solution).
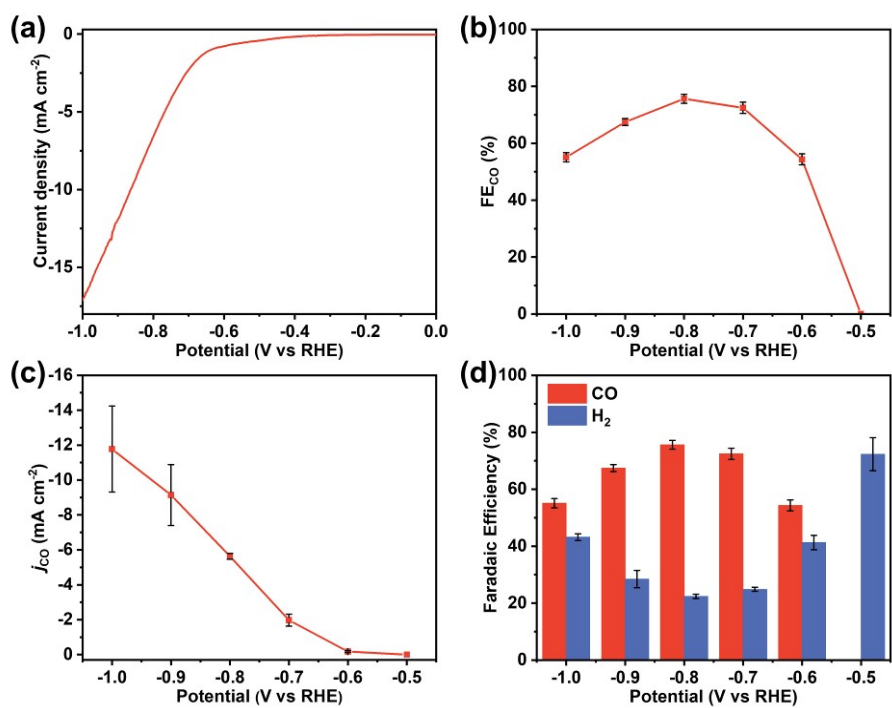
Fig. S21. (a) LSV curve, (b) FE_{CO}, (c) j_{co} and (d) FE_{CO} and FE_{H_2} of CoPor at different applied potentials in CO_2 saturated 0.5 M $KHCO_3$.
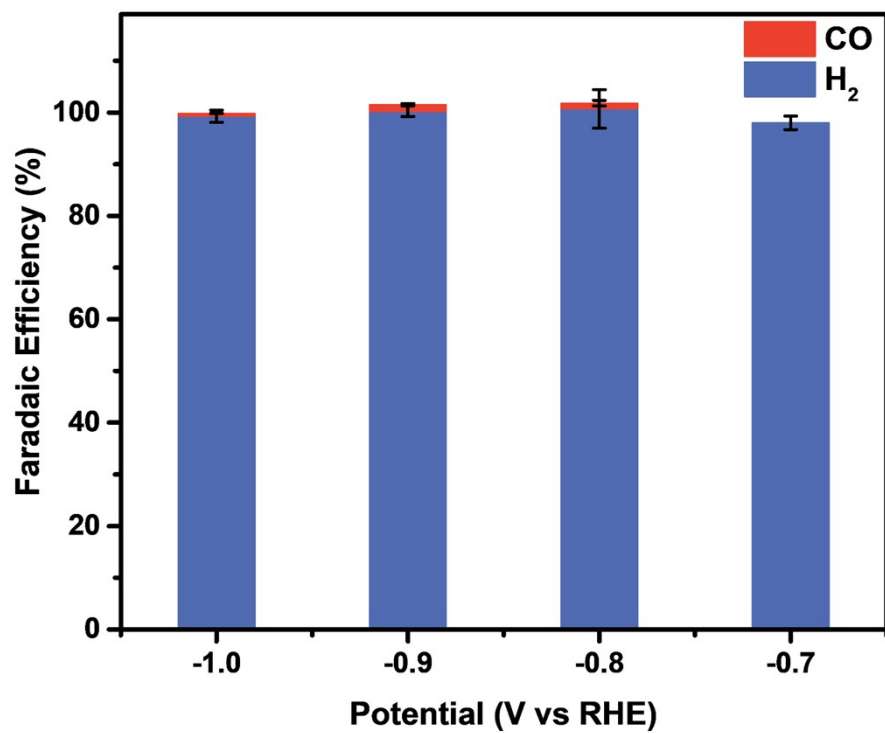
Fig. S22. FE_{CO} and FE_{H_2} of TPPDA at different applied potentials in CO_2 saturated 0.5 M $KHCO_3$.
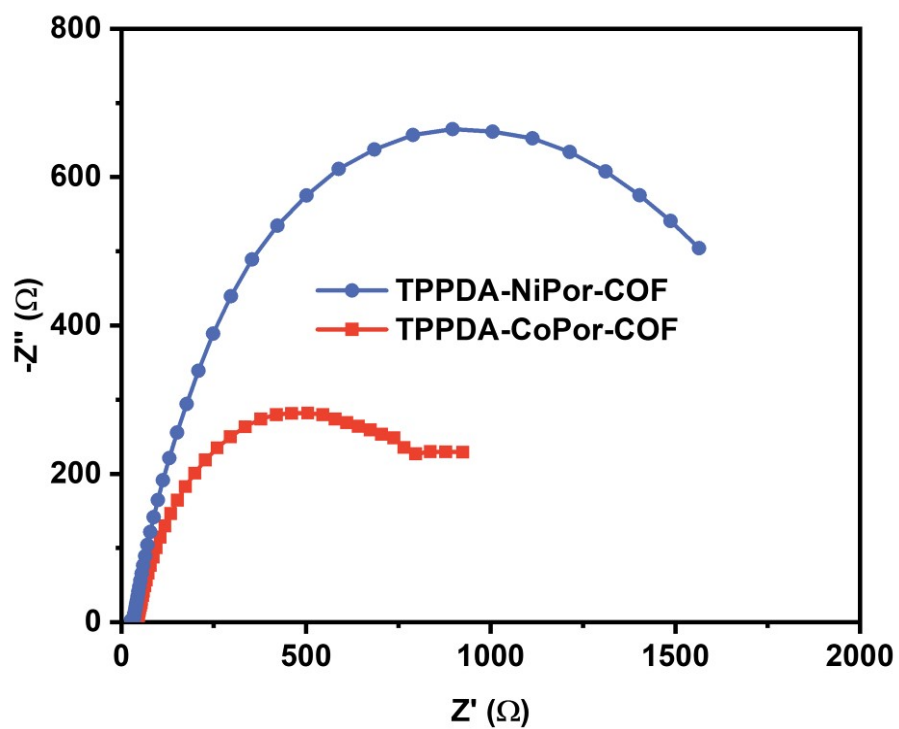
Fig. S23. Nyquist plots of EIS data for TPPDA-MPor-COFs.
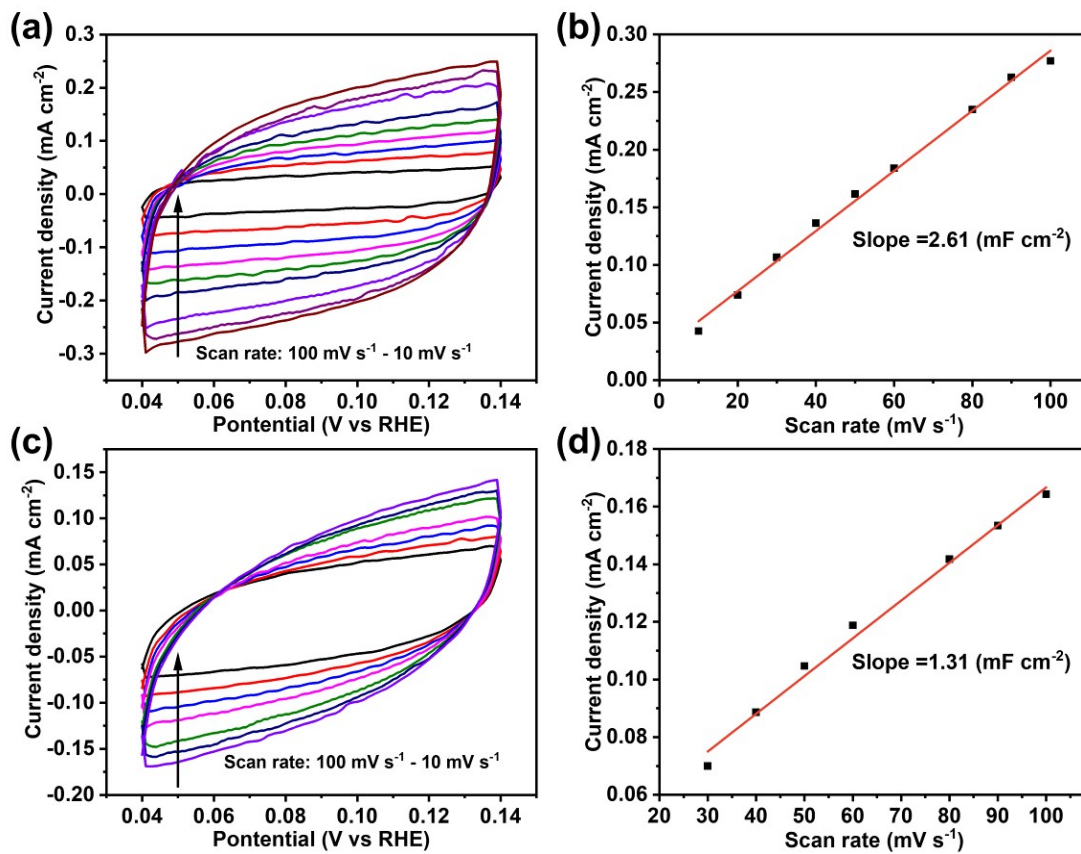
Fig. S24. Cyclic voltammogram (CV) curves in the region from 0.04 to 0.14 V vs RHE at various scan rates (from 10 to 100 mV s^{-1}) and corresponding capacitive current at 0.05 V for TPPDA-CoPor-COF (a, b) and TPPDA-NiPor-COF (c, d).
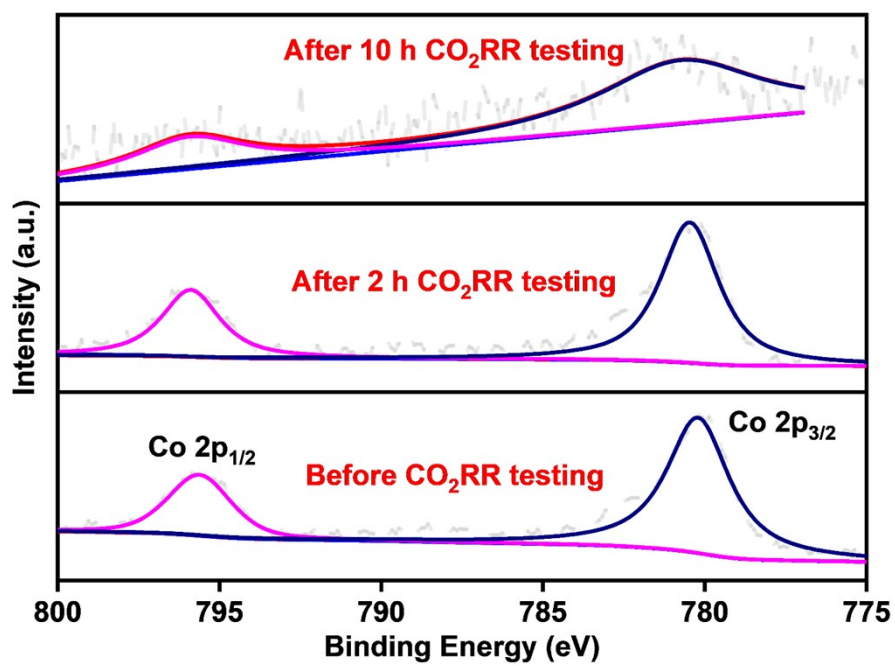
Fig. S25. XPS high-resolution scan of Co 2p for TPPDA-CoPor-COF before and after CO_2RR testing.
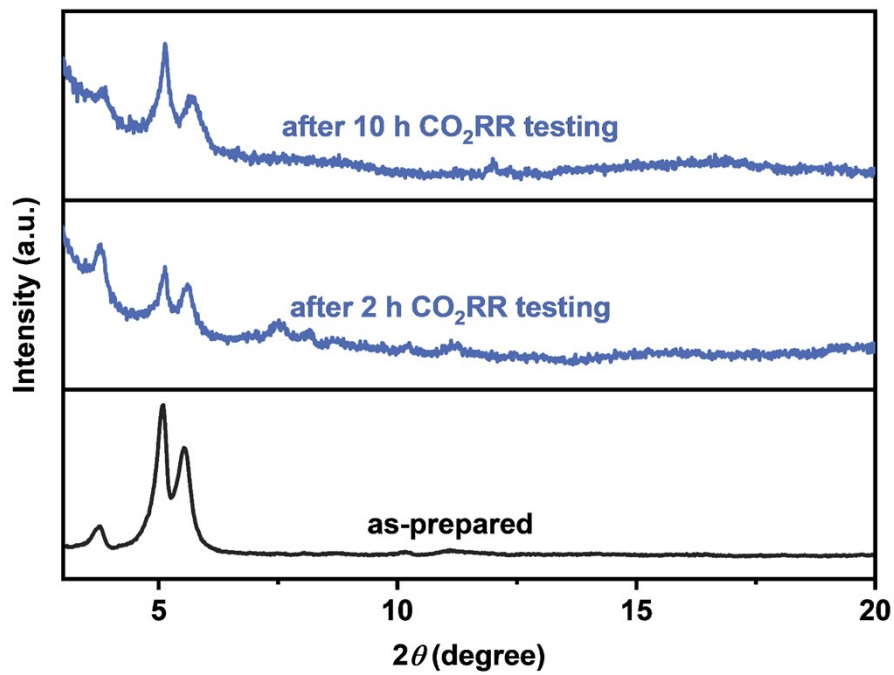
Fig. S26. PXRD patterns of TPPDA-CoPor-COF before and after CO_2RR testing.
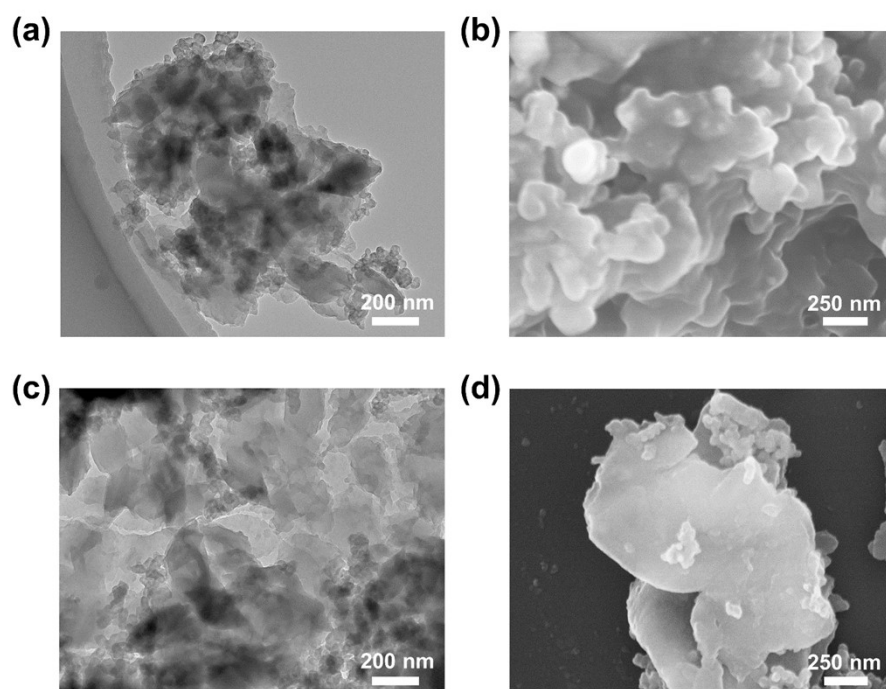
Fig. S27. (a) The TEM and (b) SEM images of TPPDA-CoPor-COF after 2 h CO$_2$RR testing, (c) The TEM and (d) SEM images of TPPDA-CoPor-COF after 10 h CO$_2$RR testing.
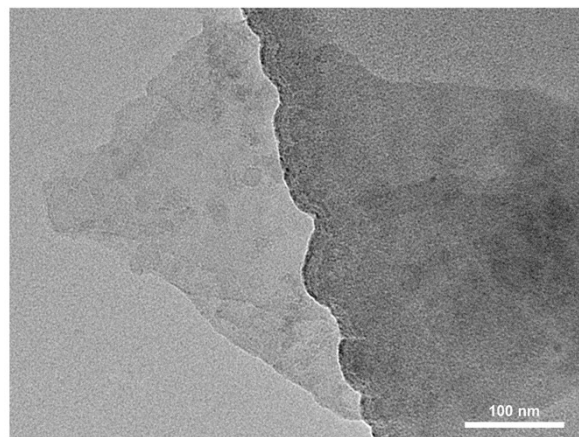
Fig. S28. The TEM image of TPPDA-CoPor-COF nanosheets.
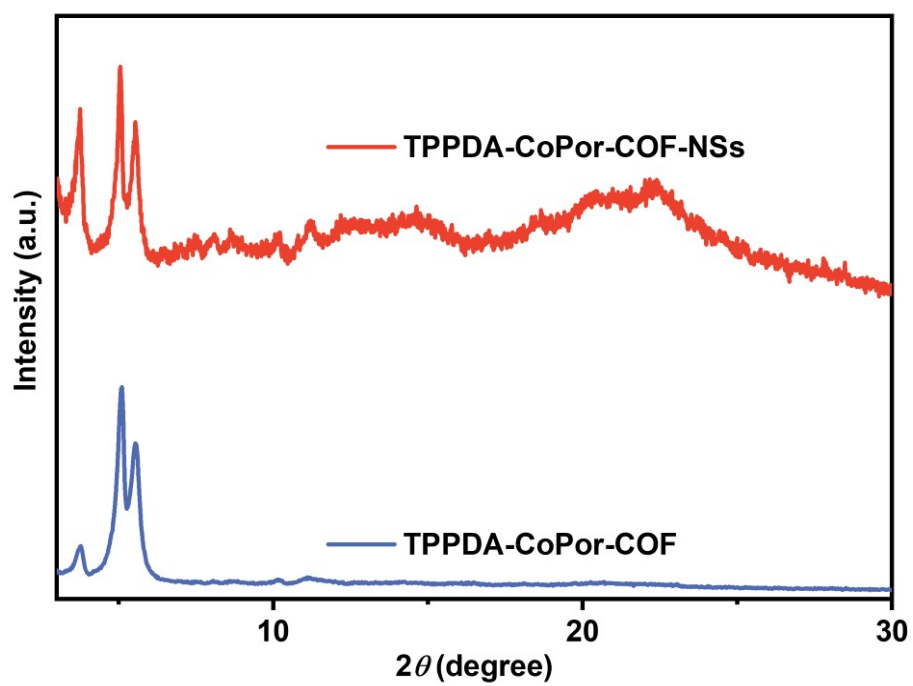
Fig. S29. PXRD patterns of TPPDA-CoPor-COF nanosheets and the as-prepared one.
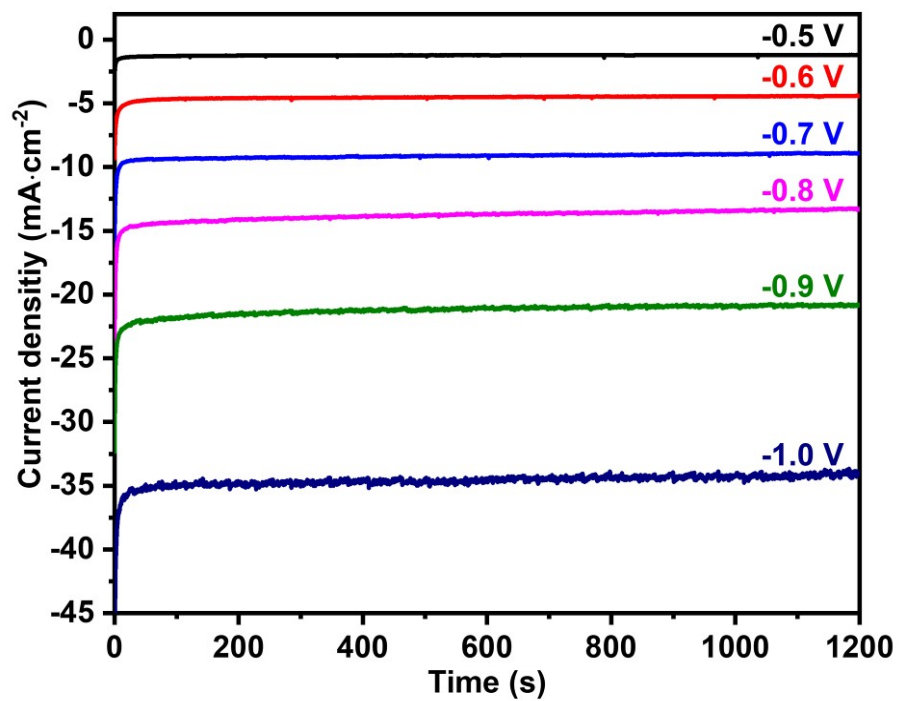
Fig. S30. Chronoamperometric responses of TPPDA-CoPor-COF nanosheets at different potentials.
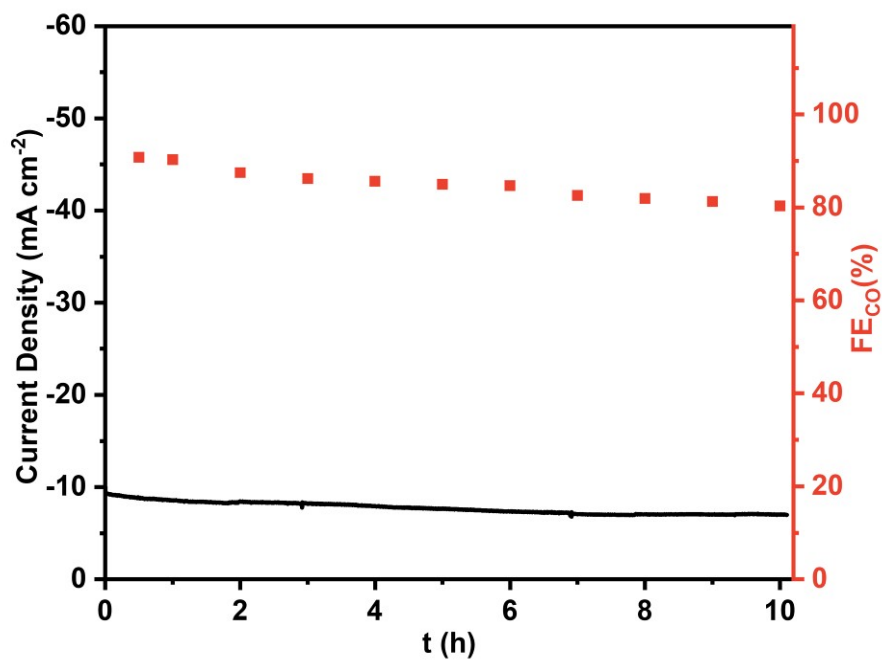
Fig. S31. Lasting stability test of TPPDA-CoPor-COF nanosheets at -0.7 V.
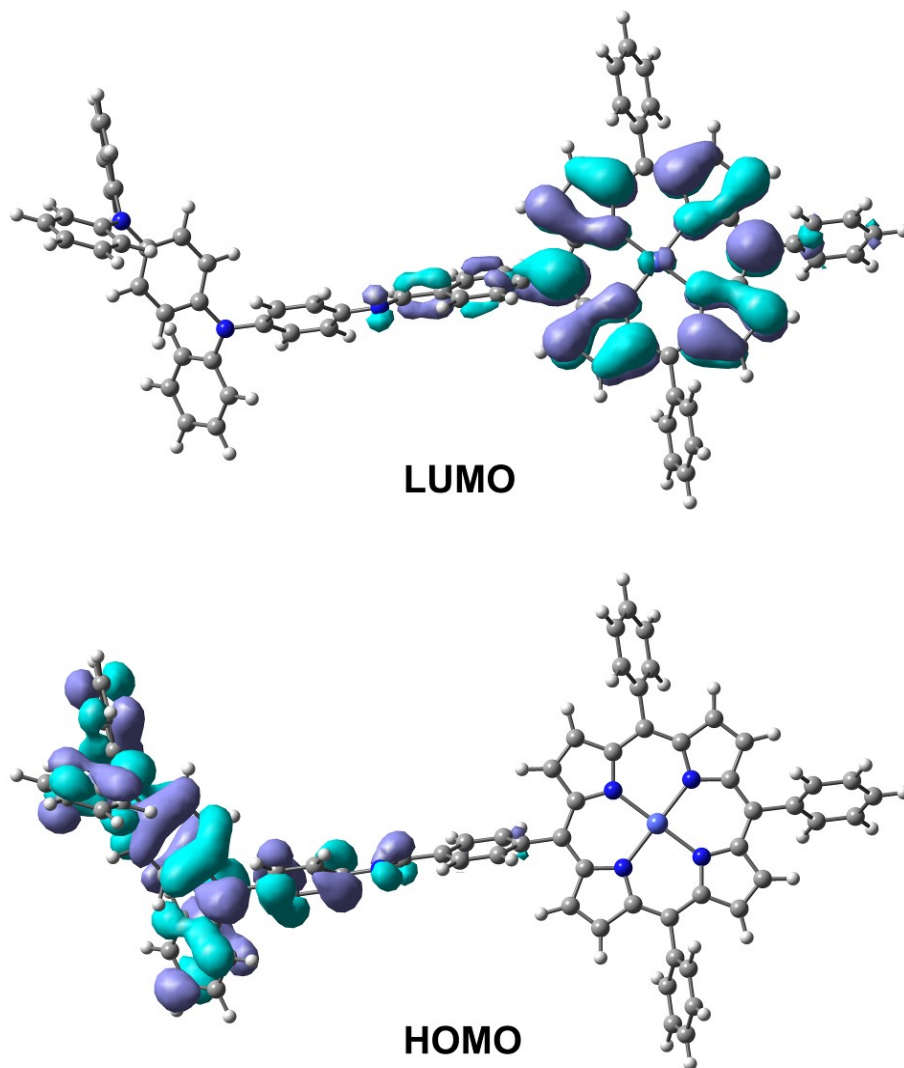
Fig. S32. The calculated LUMO and HOMO populations of the repeat unit in TPPDA-

CoPor-COF (the isovalue of the surface is 0.02).
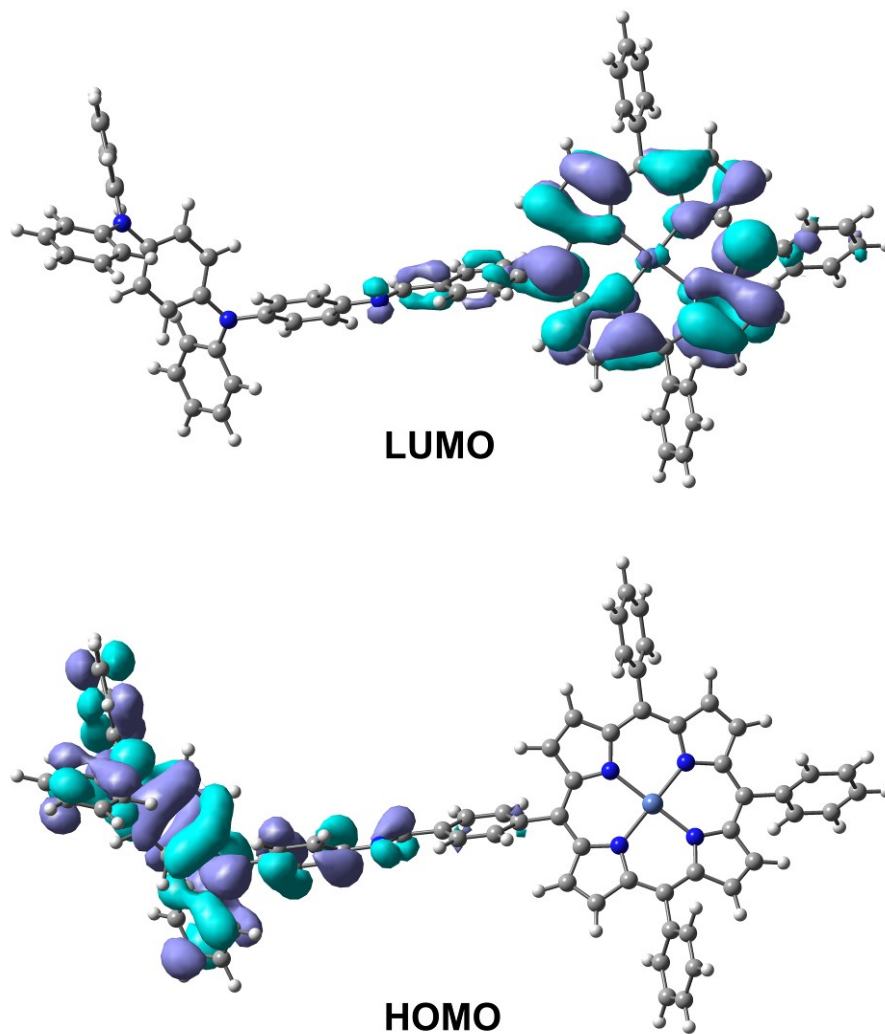
LUMO

HOMO

Fig. S33. The calculated LUMO and HOMO populations of the repeat unit in TPPDA-

NiPor-COF (the isovalue of the surface is 0.02).
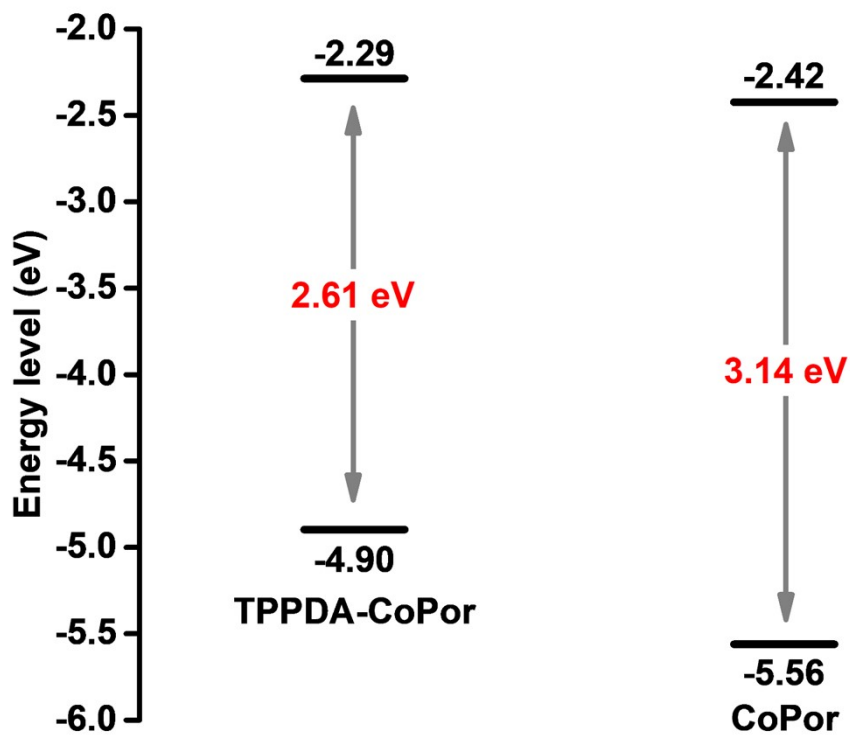
Fig. S34. The calculated LUMO and HOMO levels and gaps of the repeat unit in

TPPDA-CoPor-COF and CoPor monomer.

Table S1. Metal contents of TPPDA-MPor-COFs calculated from ICP tests.

Sample	Calculated (wt%)	Found (wt%)
TPPDA-CoPor-COF	4.98	3.35
TPPDA-NiPor-COF	4.96	3.20

Table S2. Fitting parameters for the EXAFS data of TPPDA-MPor-COFs. (CN, coordination number; R, distance between absorber and backscatter atoms; σ^2, Debye-Waller factor; R factor is used to evaluate the goodness of fitting).

Sample	Path	CN	R(Å)	$\sigma^2(10^{-3}\,\text{Å}^2)$	R factor
TPPDA-CoPor-COF	Co-N	4	1.92	4.5±5.3	0.02
TPPDA-NiPor-COF	Ni-N	4	1.93	7.1±8.7	0.02

Table S3. Comparison of the electrocatalytic performance for COF-based electrocatalysts in H-cells (0.5 M $KHCO_3$ aqueous solution).

Catalysts	Potential (V vs. RHE)	j_{CO} (mA cm^{-2})	FE$_{CO}$ (%)	Ref
TPPDA-CoPor-COF-NSs	-1.0	-29.2	87	
TPPDA-CoPor-COF	-1.0	-22.2	79	this work
TPPDA-CoPor-COF	-0.9	-15.3	90	
TT-Por(Co)-COF	-0.7	-7.28	85	S12
TTF-Por(Co)-COF	-0.9	-6.88	78.5	S13
Co-TTCOF	-0.9	-4.2	59.5	S14
COF-366-Co	-0.67	-1.8	90	
COF-367-Co	-0.67	-3.3	91	S15
COF-367-Co(1%)	-0.67	-0.4	40	
COF-367-Co(10%)	-0.67	-0.8	70	
COF-300	-0.85	-0.13	53	S16
COF-300-AR	-0.85	-1.82	80	
TAPP(Co)-B18C6-COF	-1.0	-9.45	71.5	S17

REFERENCES

1 R. Chen, Y. Wang, Y. Ma, A. Mal, X. Gao, L. Gao, L. Qiao, X. Li, L. Wu and C. Wang, Rational Design of Isostructural 2D Porphyrin-Based Covalent Organic Frameworks for Tunable Photocatalytic Hydrogen Evolution, *Nat. Commun.*, 2021, **12**, 1354.

2 C. Adamo and V. Barone, Toward Reliable Density Functional Methods without Adjustable Parameters: the PBE0 Model. *J. Chem. Phys.* **1999**,*110*, 6158–6170.

3 S. Grimme, S. Ehrlich and L. Goerigk, Effect of the Damping Function in Dispersion Corrected Density Functional Theory. *J. Comput. Chem.* **2011**, *32*, 1456–1465.

4 D. Andrae, U. Häußermann, M. Dolg, H. Stoll and H. Preuß, Energy-Adjusted Ab Initio Pseudopotentials for the Second and Third Row Transition Elements. *Theor. Chim. Acta* **1990,** *77*, 123–141.

5 P. C. Hariharan and J. A. Pople, The Influence of Polarization Functions on Molecular Orbital Hydrogenation Energies. *Theor. Chim. Acta* **1973**, *28*, 213–222.

6 M. S. Gordon, The Isomers of Silacyclopropane. *Chem. Phys. Lett.* **1980** *76*, 163–168.

7 R. Binning and L. Curtiss, Compact Contracted Basis Sets for Third-Row Atoms: Ga–Kr. *J. Comput. Chem.* **1990**, *11*, 1206–1216.

8 M. J. Frisch, G. W. Trucks, H. B. Schlegel, G. E. Scuseria, M. A. Robb, J. R. Cheeseman, G. Scalmani, V. Barone, B. Mennucci, G. A. Petersson, H. Nakatsuji, M. Caricato, X. Li, H. P. Hratchian, A. F. Izmaylov, J. Bloino, G. Zheng, J. L. Sonnenberg, M. Hada, M. Ehara, K. Toyota, R. Fukuda, J. Hasegawa, M. Ishida, T. Nakajima, Y.

Honda, O. Kitao, H. Nakai, T. Vreven, J. A. Montgomery, Jr., J. E. Peralta, F. Ogliaro, M. Bearpark, J. J. Heyd, E. Brothers, K. N. Kudin, V. N. Staroverov, T. Keith, R. Kobayashi, J. Normand, K. Raghavachari, A. Rendell, J. C. Burant, S. S. Iyengar, J. Tomasi, M. Cossi, N. Rega, J. M. Millam, M. Klene, J. E. Knox, J. B. Cross, V. Bakken, C. Adamo, J. Jaramillo, R. Gomperts, R. E. Stratmann, O. Yazyev, A. J. Austin, R. Cammi, C. Pomelli, J. W. Ochterski, R. L. Martin, K. Morokuma, V. G. Zakrzewski, G. A. Voth, P. Salvador, J. J. Dannenberg, S. Dapprich, A. D. Daniels, O. Farkas, J. B. Foresman, J. V. Ortiz, J. Cioslowski, and D. J. Fox, Gaussian 09, Version D.01, Gaussian, Inc., Wallingford CT, **2013**.

9 A. V. Marenich, C. J. Cramer and D. G. Truhlar, Universal solvation model based on solute electron density and on a continuum model of the solvent defined by the bulk dielectric constant and atomic surface tensions, *J. Phys. Chem. B*, 2009, **113**, 6378-6396.

10 K. Chan and J. K. Nøskov, Electrochemical Barriers Made Simple. *J. Phys. Chem. Lett.* **2015**, *6*, 2663–2668.

11 A. A. Peterson, F. Abild-Pedersen, F. Studt, J. Rossmeisl, and J. K. Nøskov, How Copper Catalyzes the Electroreduction of Carbon Dioxide into Hydrocarbon Fuels. *Energy Environ. Sci.* **2010**, *3*, 1311–1315.

12 Q. Wu, M. J. Mao, Q. J. Wu, J. Liang, Y. B. Huang and R. Cao, Construction of Donor–Acceptor Heterojunctions in Covalent Organic Framework for Enhanced CO_2 Electroreduction, *Small*, 2021, **17**, 2004933.

13 Q. Wu, R. Xie, M. Mao, G. Chai, J. Yi, S. Zhao, Y. Huang and R. Cao, Integration

of Strong Electron Transporter Tetrathiafulvalene into Metalloporphyrin-Based Covalent Organic Framework for Highly Efficient Electroreduction of CO_2, *ACS Energy Letters*, 2020, **5**, 1005-1012.

14 H. Zhu, M. Lu, Y. Wang, S. Yao, M. Zhang, Y. Kan, J. Liu, Y. Chen, S. Li and Y. Lan, Efficient electron transmission in covalent organic framework nanosheets for highly active electrocatalytic carbon dioxide reduction, *Nat. Commun.*, 2020, **11**, 497.

15 S. Lin, C. S. Diercks, Y. B. Zhang, N. Kornienko, E. M. Nichols, Y. Zhao, A. R. Paris, D. Kim, P. Yang, O. M. Yaghi and C. J. Chang, Covalent organic frameworks comprising cobalt porphyrins for catalytic CO_2 reduction in water, *Science*, 2015, **349**, 1208-1213.

16 H. Liu, J. Chu, Z. Yin, X. Cai, L. Zhuang and H. Deng, Covalent Organic Frameworks Linked by Amine Bonding for Concerted Electrochemical Reduction of CO_2, *Chem*, 2018, **4**, 1696-1709.

17 S. An, C. Lu, Q. Xu, C. Lian, C. Peng, J. Hu, X. Zhuang and H. Liu, Constructing Catalytic Crown Ether-Based Covalent Organic Frameworks for Electroreduction of CO_2, *ACS Energy Letters*, 2021, **6**, 3496-3502.